Research Square

Preprints are preliminary reports that have not undergone peer review.
They should not be considered conclusive, used to inform clinical practice,
or referenced by the media as validated information.

Geometry-dependent probabilistic line-of-response weighting for inter-crystal scatter events in PET

Hyeong Seok Shim
Korea Advanced Institute of Science and Technology
Muhammad Nasir Ullah
Stanford University
Jae Sung Lee
Seoul National University
Craig S. Levin
Stanford University
Guen Bae Ko
guenbko@kaist.ac.kr

Korea Advanced Institute of Science and Technology

Article

Keywords:

Posted Date: November 16th, 2026

DOI: https://doi.org/10.21203/rs.3.rs-11550280/v1

License: This work is licensed under a Creative Commons Attribution 4.0 International License.
Read Full License

Additional Declarations: No competing interests reported.

Geometry-dependent probabilistic line-of-response weighting for inter-crystal scatter events in PET

Hyeong Seok Shim[1,2], Muhammad Nasir Ullah[3], Jae Sung Lee[4,5,6], *Craig S. Levin[3] and *Guen Bae Ko[1]

[1]Department of Nuclear and Quantum Engineering, Korea Advanced Institute of Science and Technology, Daejeon, Republic of Korea

[2]Mechanical Engineering Research Institute, Korea Advanced Institute of Science and Technology, Daejeon, Republic of Korea

[3]Department of Radiology, Molecular Imaging Program, Stanford University, Stanford, United States of America

[4]Interdisciplinary Program in Bioengineering, College of Engineering, Seoul National University, Seoul, Republic of Korea

[5]Integrated Major in Innovative Medical Science, Seoul National University, Seoul, Republic of Korea

[6]Department of Nuclear Medicine, Seoul National University College of Medicine, Seoul, Republic of Korea

*co-senior authors

Corresponding author: Guen Bae Ko (guenbko@kaist.ac.kr)

Abstract

Inter-crystal scatter often distributes the energy of an annihilation photon across two crystals and leaves two candidate lines of response (LORs) that conventional detectors cannot reliably distinguish. Dividing the count between the two lines avoids this decision, but existing proportional weights depend on the activity distribution of each acquisition. Here we derive the weight from the detector geometry instead. In GATE simulations of the PET*coil* brain insert, we tabulated from a 180 s normalization acquisition the probability that the crystal with the larger energy is the first interaction crystal, against crystal separation and opposing crystal position. The probability fell from 0.40 for adjacent crystals to 0.05 at 14.6 mm and differed by a factor of 1.8 between the two sides of the scattering crystal at oblique incidence. Two implementations were evaluated: a geometry-dependent table and its event-weighted mean as a constant weight. Both implementations improved LOR count accuracy over conventional assignments in uniform, hot–cold and Hoffman phantoms and performed equally across them. After 1200 s of the uniform phantom, the table gave a count error of 22.4%, against 26.9% for the lower energy assignment. In Hoffman images, it raised the gray matter signal-to-noise ratio from 5.09 to 7.52.

Introduction

Positron emission tomography (PET) is a medical imaging technique that detects 511 kev photons emitted from within the patient's body following the administration of a radioactive isotope, using scintillation crystals coupled to photosensors. The crystal width is chosen according to the target[1–5], and as it decreases the proportion of inter-crystal scattering (ICS) increases[6–9]. In ICS, an annihilation photon Compton-scatters from one crystal into another crystal of the same block, so that the energy is shared between two positions. Although ICS can involve energy deposition in more than two crystals, two-crystal ICS events constitute a major class of such events[10]. Accordingly, many ICS positioning methods focus on two-crystal events, often assuming a single Compton scattering interaction followed by absorption in the second crystal. The position at which the photon first interacts carries the directional information, and it is this position that defines the correct line of response (LOR). Assigning the event to the wrong crystal places a count on a false LOR and degrades the reconstructed image quality, while rejecting ICS events altogether costs sensitivity that small-crystal systems can ill afford[11–13]. A number of methods[10] have been proposed to recover the first interaction crystal from the energy distribution[14–20], from depth-of-interaction (DOI) measurements[21–24], or from Compton kinematics[25–27], but in scintillation detectors, achieving an accuracy beyond approximately 80% on the scattered events themselves has remained challenging[14,16,18,21]. The limitation is not solely algorithmic, but is fundamentally constrained by the information available from the detector. Compton kinematics relates the scattering angle uniquely to the deposited energies, but recovering that angle demands energy and position measurements considerably finer than current detectors provide. Within a single block the two interaction sites lie only a few millimeters apart, so that the finite spatial resolution of the measured positions translates into substantial uncertainty in the inferred Compton scattering angle. Consequently, the first interaction crystal can remain ambiguous from the available observables, limiting the accuracy achievable by classification alone.

An alternative is therefore not to choose a single crystal, but to determine how the count should be divided between the two candidate LORs. Several methods have been proposed along these lines, assigning weights to the two LORs rather than selecting one of them[12,16,28,29]. Each two-crystal ICS event admits exactly two candidates and the count may be distributed between them with weights summing to unity. The deterministic assignments are recovered when one weight is set to one. What distinguishes such methods is how the weights are obtained. Equal weights of 0.5 are simple to apply but take no account of the physics[16]. The proportional method instead uses the ratio of photoelectric events recorded in each LOR and yields a clear improvement in image quality[12], but that ratio depends on the activity distribution and therefore on the subject. The weights must then be re-derived from each acquisition, which favors histogram-mode reconstruction and makes direct application to streaming list-mode data

less practical. Moreover, the relative frequencies of photoelectric events do not necessarily reflect the first interaction probabilities of ICS events, as the two event types involve different interaction processes.

We propose weights that depend on the system geometry rather than on the activity distribution. The probability that the first interaction occurred in a particular crystal is governed by the Klein–Nishina differential cross section and by the attenuation along the path between the two crystals, both of which are determined by the detector configuration rather than by the scanned object and its activity distribution. Conditioned on the geometric relationship between the two interacting crystals and the opposing crystal, the weight is thus target-independent: it is a property of the scanner and remains valid across subjects and activity distributions. The weights can be precomputed for each geometric configuration using Monte Carlo simulations once and applied to list-mode data as the events arrive.

In this study, we evaluate the proposed method using a simulated PET*coil* brain PET system[30,31] comprising 16 detector modules per ring, each containing a 16 × 8 array of LYSO crystals (3.2 × 3.2 × 20 mm^3) with a pitch of 3.26 mm. We define the conditional probability (p) that the crystal with the higher deposited energy is the first interaction crystal for a given geometric configuration. This probability is estimated from a simulated normalization acquisition and tabulated according to the transaxial and axial separations between the interacting crystals and the position of the opposing crystal. The resulting probability table is then used to distribute each ICS event between its two candidate LORs. We evaluate the method using three phantoms with different activity distributions, comparing the recovered LOR counts with those obtained using conventional assignment and weighting methods across acquisition times. We also examine the effect of estimating the probability table from the target acquisition rather than from a separate normalization acquisition. Finally, Hoffman brain phantom images are reconstructed to assess image quality and agreement with images obtained using the true first interaction crystals.

Results

Geometry-Dependent ICS probability

The geometry-dependent probability (p), representing the probability that the higher-energy crystal was the first interaction crystal, was estimated from a simulated normalization acquisition and tabulated according to the transaxial and axial separations between the two interacting crystals and the position of the opposing crystal. The 180 s normalization acquisition provided 1.07×10^8 ICS events within the energy window. Over all geometric configurations, the crystal that recorded the larger energy was the first interaction crystal in 32.6% of events ($\bar{p} = 0.326$). The standard deviation of p across configurations, weighted by events, was 0.12.

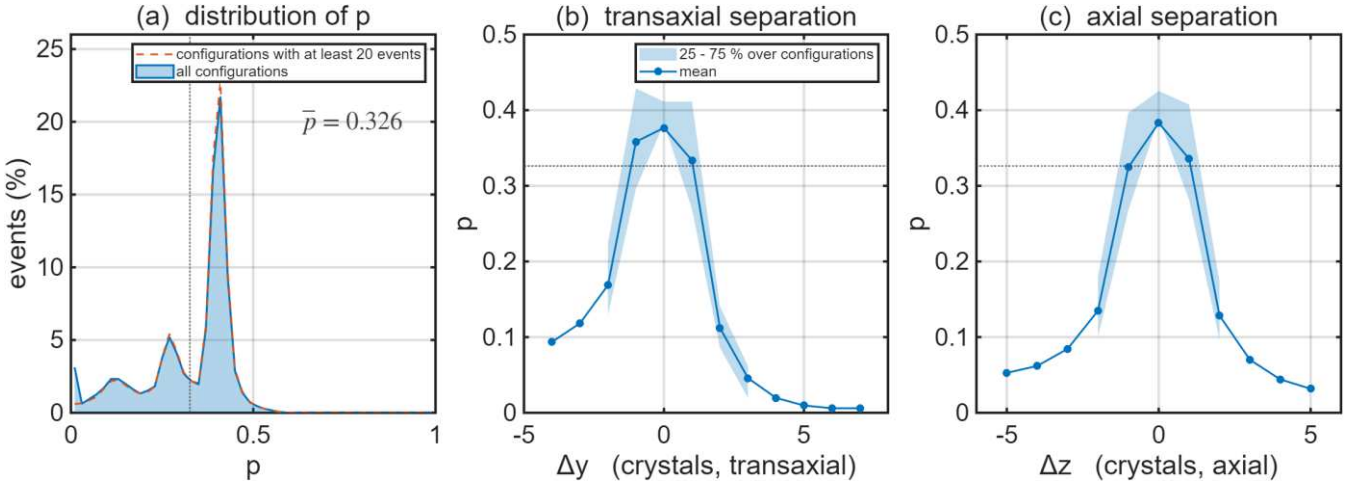


Figure 1. Probability p from the 180 s normalization acquisition. (a) Event weighted distribution of p for all configurations and for configurations with at least 20 events. (b) p against transaxial separation. (c) p against axial separation

The number of events per configuration is highly uneven. Many configurations hold only a few events, and their estimates of p take only a few discrete values. Figure 1a shows the distribution of p, weighted by events, over all configurations and over configurations with at least 20 events. Configurations with at least 20 events hold 95.2% of the events. The two distributions are nearly identical and differ mainly below p = 0.02, which holds 3.1% of events over all configurations and 0.6% over configurations with at least 20 events. For a configuration with 20 events the standard error of p near its mean is about 0.1, so part of the width of both distributions comes from estimation noise. The distribution peaks near p = 0.41, where 21.7% of events lie.

Figures 1b,c show p as a function of the transaxial and the axial separation between the two crystals that share the energy. Both profiles are highest at zero separation, 0.377 transaxially and 0.383 axially, and fall to 0.046 and 0.070 at a separation of +3 crystals. Separations of at most one crystal hold 88.4% of events transaxially and 89.6% axially, and the remaining events are spread over many sparsely populated configurations. The transaxial profile is not symmetric, and at a separation of −3 crystals p was

0.118. The sign of the separation is taken relative to the direction of incidence, with a positive sign placing the lower energy crystal on the side from which the annihilation photon arrives, and at oblique incidence the photon reaches the crystal on that side first (Fig. 2e).

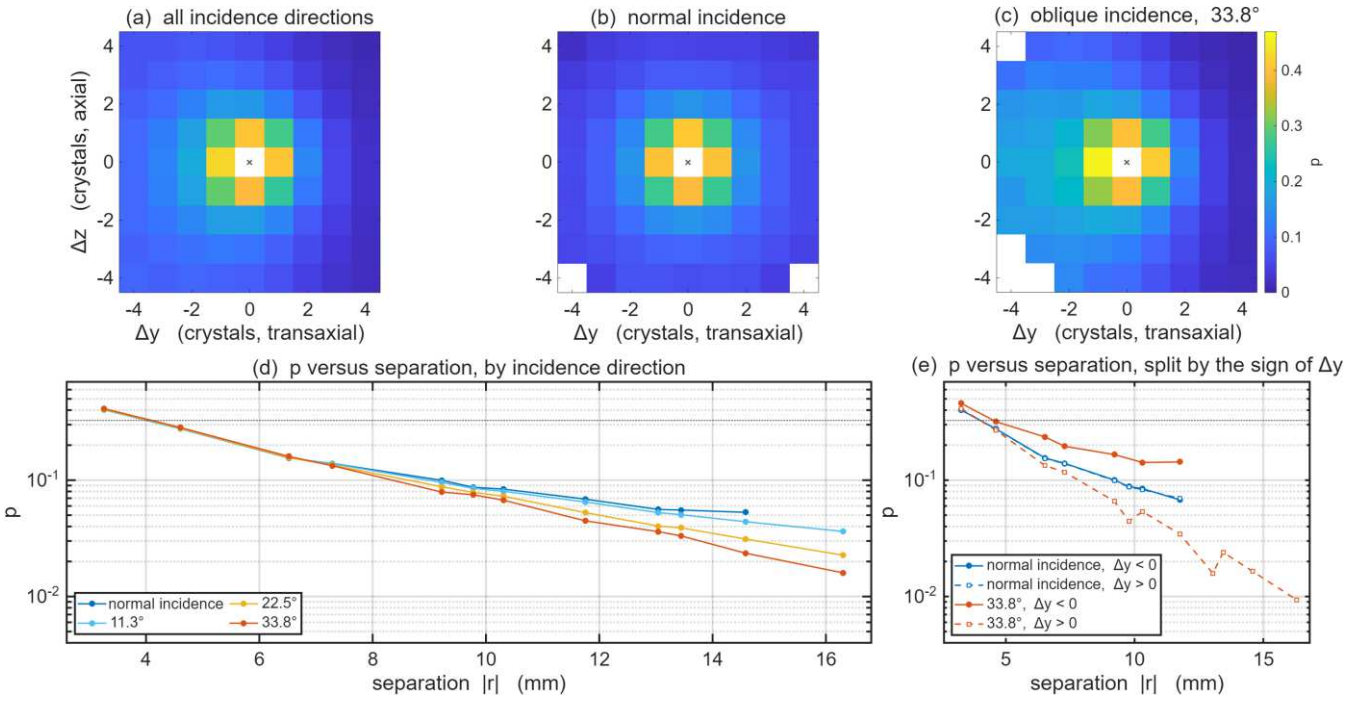


Figure 2. Dependence of p on the position of the opposing crystal. (a) p over the plane of transaxial and axial separation for all incidence directions. (b) Normal incidence. (c) Incidence angle of 33.8°. (d) p against the distance between crystal centers for four module offsets. (e) p against distance for the two signs of the transaxial separation

Figures 2a–c show p over the plane of transaxial and axial separation, for all incidence directions (a), for normal incidence (b) and for an incidence angle of 33.8° (c). Cells with fewer than 500 events are left blank. On a ring of 16 modules, the module offset of the opposing crystal sets the direction from which the annihilation photon arrives. An offset of eight corresponds to normal incidence on the detector face, and an offset of five to an incidence angle of 33.8°. Figure 2d shows p as a function of the distance between the two crystal centers for four such offsets. The distance takes only the values allowed by the crystal grid, so the points are unevenly spaced. Under normal incidence p fell from 0.402 at one crystal pitch to 0.053 at 14.6 mm. The four directions gave nearly the same values up to about 8 mm and separated at larger distances. At 33.8°, p was 21% lower than at normal incidence at 9.2 mm and 55% lower at 14.6 mm.

Figure 2e shows the same dependence separately for the two signs of the transaxial separation. A positive sign places the lower energy crystal on the side from which the annihilation photon arrives. Under normal incidence the two signs agreed to within 0.002 at every distance, as expected from the symmetry. At 33.8° they differed strongly. At 6.5 mm, p was 0.235 for a negative sign and 0.133 for a positive sign, a ratio of 1.8. At oblique incidence the photon reaches the crystal on the arrival side first, so this crystal

is more likely to be the first interaction crystal. The same asymmetry appears in the axial direction but is weaker, because the axial incidence angle is mostly below 10° in this scanner. The probability therefore depends on the position of the opposing crystal and cannot be described by a weight that depends only on the two crystals that share the energy.

Evaluation of LOR assignment accuracy

To evaluate the proposed method, each ICS event was distributed between its two candidate LORs using either the geometry-dependent probability corresponding to its geometric configuration (geometric table) or a single probability ($\bar{p}$) obtained as the event-weighted mean of these probabilities (constant weighting). The resulting LOR count distributions were compared with those obtained using four reference methods: two deterministic assignments based on the lower or higher deposited energy (min-E and max-E), equal weighting (0.5), and the proportional method based on photoelectric event counts. The accuracy of each method was evaluated against the LOR counts obtained using the true first interaction crystals, using four metrics: L_1, leakage, SD (standard deviation), and RMSE (root mean square error). The table and $\bar{p}$ were estimated once from the 180 s normalization acquisition and were not re-estimated for the phantoms, whose data were used only to evaluate the methods. Figure 3 shows the evaluation metrics against the acquisition time of each phantom, from 60 to 1200 s, for the uniform, hot–cold and Hoffman phantoms. The normalized absolute error, L_1, decreased with acquisition time for every method. With the geometric table it fell from 37.3% at 60 s to 22.4% at 1200 s for the uniform phantom, from 36.5% to 19.9% for the hot–cold phantom and from 38.3% to 25.4% for the Hoffman phantom. The min-E method changed less, rising to about 36.3% between 120 and 300 s and then falling to 26.9%, 24.0% and 30.1% at 1200 s. At 60 s the min-E method was more accurate than the geometric table, by 2.5, 1.3 and 4.5 percentage points for the uniform, hot–cold and Hoffman phantoms. The geometric table overtook it after 106 s, 82 s and 166 s, in all three cases at about 1.3 true counts per LOR. Below this occupancy, most lines hold a single event, and dividing that event between two lines is necessarily wrong for one of

them. Above it, the division reproduces an occupancy that a single assignment cannot.

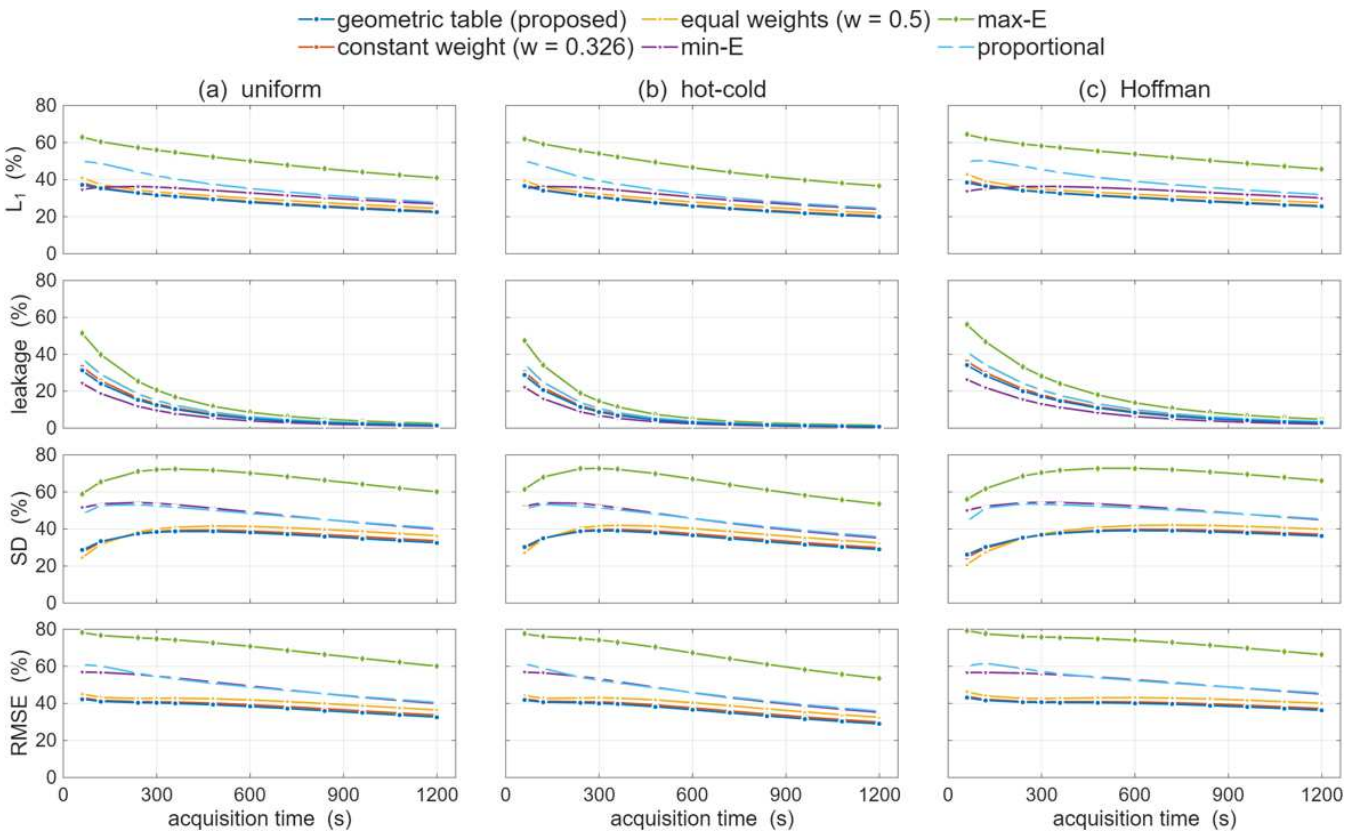


Figure 3. Evaluation quantities against acquisition time for the (a) uniform, (b) hot–cold and (c) Hoffman phantoms, with L_1, leakage, SD and RMSE from top to bottom

The decomposition of the error explains this behavior. The leakage, the weight placed on LORs that recorded no true event, decreased steeply with acquisition time for every method, from 31.2% to 1.5% for the geometric table on the uniform phantom, as fewer lines remained empty. The SD first increased, from 28.6% at 60 s to a maximum of 38.7% at 360 s, and then decreased to 32.6% at 1200 s. The RMSE therefore changed little up to 300 s, from 42.3% to 40.2%, and then fell to 32.6% at 1200 s. For the hot–cold and Hoffman phantoms it fell from 41.7% to 28.9% and from 43.0% to 36.3%. The min-E method kept an SD between 40% and 54% for the uniform phantom at all acquisition times, because committing each event to a single line produces an error of unit size whenever the choice is wrong.

At 1200 s the order of the methods was the same for the three phantoms in L_1, SD and RMSE. For the uniform phantom, L_1 was 22.4% with the geometric table, 22.9% with the constant weight, 24.6% with equal weights, 26.9% with the min-E method, 27.8% with the proportional method and 40.9% with the max-E method, and the RMSE was 32.6%, 33.6%, 36.4%, 40.0%, 40.5% and 60.1%. The improvement over deterministic assignment was therefore large, whereas that over the constant weight was small, 0.55 percentage points in L_1 and 1.04 in RMSE, a relative reduction of 3.1%. This improvement held at every acquisition time for each of the three phantoms, with a difference in L_1 between 0.16 and 1.16 percentage points. The proportional method was less accurate than equal weights at every acquisition time and, at

1200 s, less accurate than the min-E method. The min-E method gave the lowest leakage.

Compared at equal occupancy rather than at equal acquisition time, the three phantoms agreed closely. At two true counts per LOR the geometric table gave an L_1 of 30.6% for the uniform phantom, 30.7% for the hot–cold phantom and 30.8% for the Hoffman phantom, although the activity distributions range from uniform through a four to one rod contrast to a structured brain pattern. A single table estimated from a normalization acquisition therefore performed equally across activity distributions.

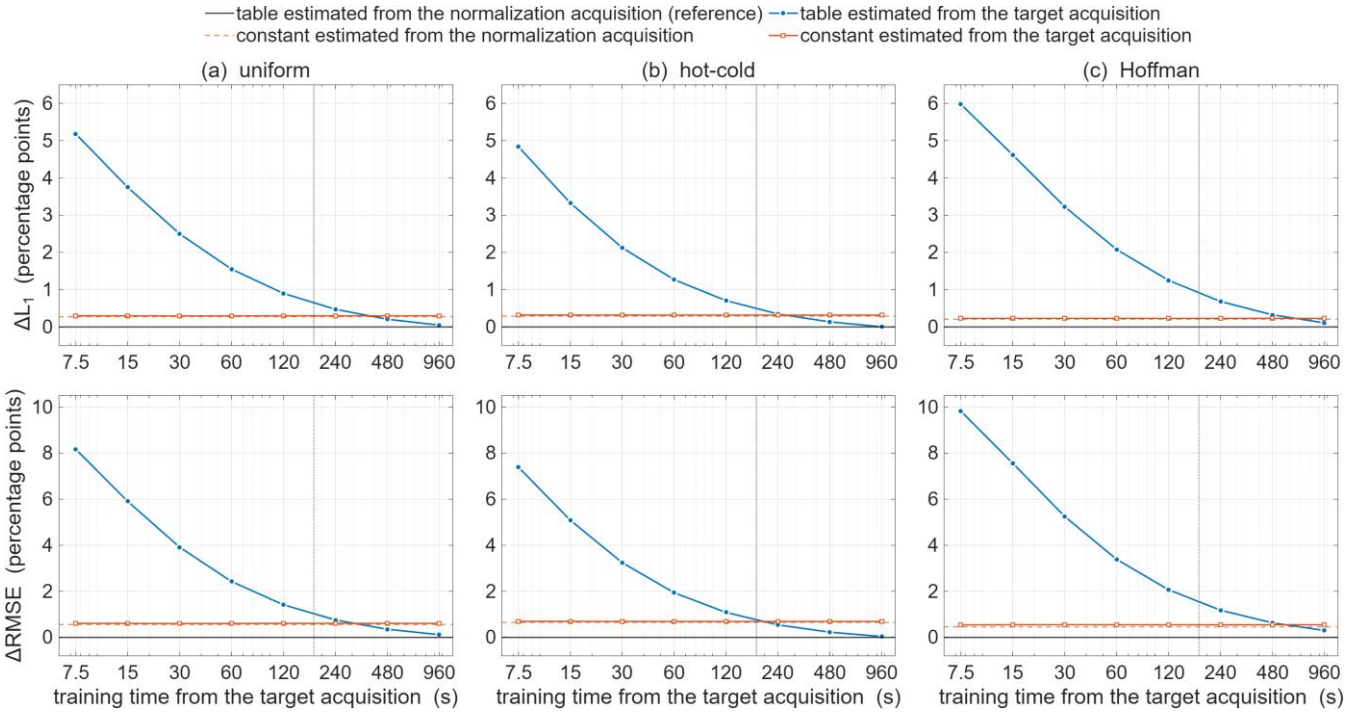


Figure 4. Accuracy of tables estimated from the target acquisition, relative to the table from the 180 s normalization acquisition (zero line), for the (a) uniform, (b) hot–cold and (c) Hoffman phantoms. ΔL_1 (top) and ΔRMSE (bottom) against training time, with testing on the last 240 s of each 1200 s acquisition

Figure 4 shows the accuracy of tables estimated from the target acquisition itself. Each 1200 s acquisition was split into the first 960 s for training and the last 240 s for testing, and all tables were scored on the same test part. The table estimated from the target acquisition improved with the training time, but it did not become more accurate than the table from the 180 s normalization acquisition. With 7.5 s of training, its L_1 exceeded that of the normalization table by 5.2, 4.8 and 6.0 percentage points for the uniform, hot–cold and Hoffman phantoms. With 960 s of training, more than five times the length of the normalization acquisition, the excess was 0.05, 0.004 and 0.11 percentage points in L_1 and 0.12, 0.04 and 0.30 percentage points in RMSE. The table estimated from the target acquisition became more accurate than the constant estimated from the same data only after 480 s of training for the uniform and hot–cold phantoms and after 960 s for the Hoffman phantom.

The coverage of the table explains this order. A phantom populates geometric configurations in proportion to its activity distribution rather than uniformly, so a table estimated from it is incomplete. The

fraction of test events whose configuration was present in the table increased from 69–80% after 7.5 s of training to above 99% after 960 s, and the remaining events were assigned the constant of the training data. A single 180 s normalization acquisition, in which every configuration is populated by construction, therefore gave the same accuracy as about 960 s of the target acquisition.

Image Quality Evaluation

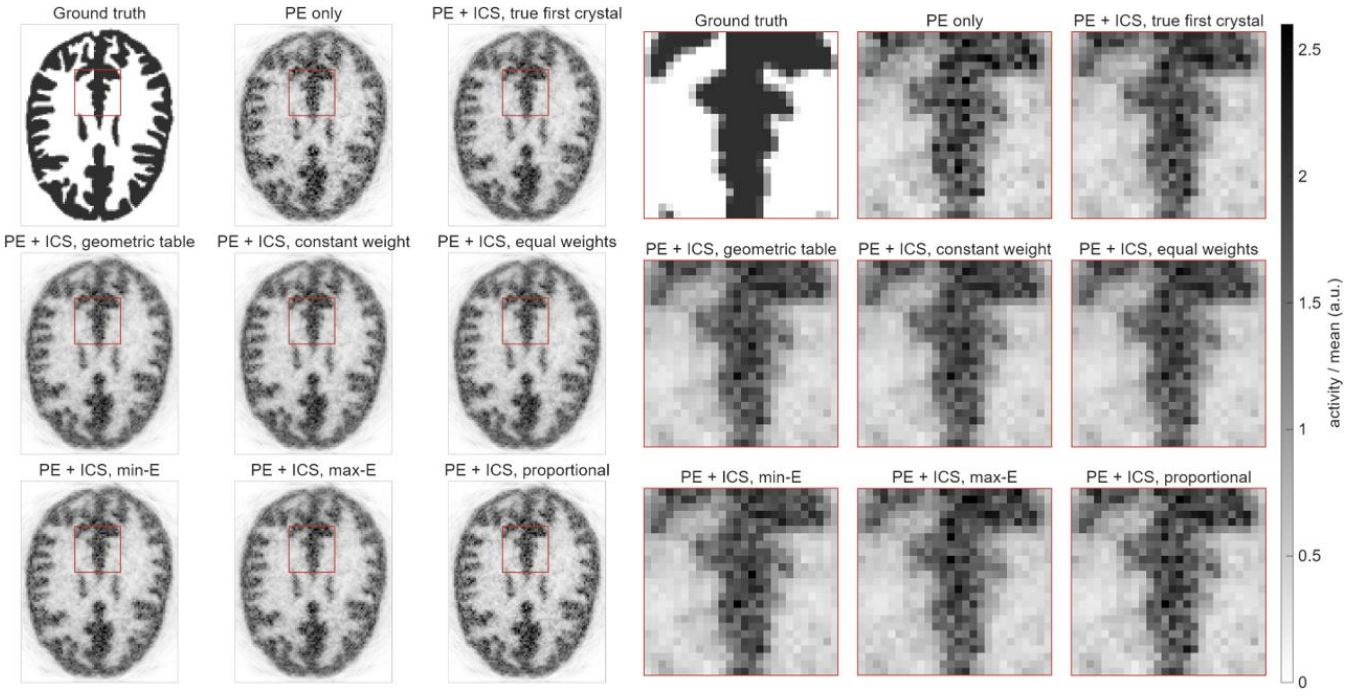


Figure 5. Central slice of the reconstructed Hoffman phantom, 1200 s, seven iterations of OSEM (ordered subset expectation maximization) with 8 subsets and 1.6 mm voxels. (a) Whole slice. (b) 40 mm by 40 mm region in the red square of (a)

To evaluate the impact of ICS event weighting on reconstructed image quality, Hoffman brain phantom images were reconstructed using photoelectric events alone and with ICS events added using each of the six weighting methods. Images reconstructed using the true first interaction crystals were also included as a reference. Figure 5 shows the central slice of the Hoffman phantom reconstructed from 1200 s of data after seven iterations. Adding the ICS events to the photoelectric events visibly reduced the noise for every assignment method. The images obtained with the different assignment methods were difficult to distinguish by visual inspection. The differences between the methods appeared in the quantitative measures below.

The ICS events added 76% to the photoelectric counts at every acquisition time, with 4.36×10^7 ICS events and 5.70×10^7 photoelectric events at 1200 s. The gray matter SNR (signal-to-noise ratio) rose from 5.09 with photoelectric events alone to 6.79 with the true first interaction crystal and to 7.52 with the geometric table at seven iterations, and it was higher with the ICS events at every iteration (Fig. 6a).

The geometric table gave a higher SNR than the true first interaction crystal because dividing each event between two lines lowers the variance of the counts.

At seven iterations, adding the ICS events improved the SSIM (structural similarity index measure) by 6.1% with the true first interaction crystal, 5.3% with the geometric table, 4.8% with the constant weight, 4.7% with the min-E method, 4.6% with the proportional method, 4.3% with equal weights and 1.0% with the max-E method (Fig. 6b). The max-E method gave a lower SSIM than photoelectric events alone up to five iterations, and equal weights did so up to two iterations. The improvement grew with the number of iterations, because the noise of photoelectric events alone grew faster.

To isolate the effect of the assignment, each image was compared with the image reconstructed from the same events with the true first interaction crystal (Fig. 6c,d). The geometric table gave the smallest MAE (mean absolute error) and the largest Dice coefficient among the practical methods at every acquisition time. At 1200 s, the MAE was 0.056 for the geometric table, 0.058 for the constant weight, 0.063 for equal weights, 0.069 for the min-E method, 0.076 for the proportional method, 0.106 for the max-E method and 0.117 for photoelectric events alone. The Dice coefficient was 0.975, 0.974, 0.971, 0.969, 0.965, 0.950 and 0.942 in the same order. The geometric table reduced the MAE of photoelectric events alone by about half at every acquisition time. The geometric table ranked first in both measures at every iteration from 1 to 15 and at every acquisition time.

Adding the ICS events with the geometric table increased the CNR (contrast-to-noise ratio) between gray matter and white matter by 51% at 1200 s, from 7.16 to 10.80 (Fig. 6e). With the ICS events added, 600 s of data gave a CNR of 7.67 with the geometric table, higher than the 7.16 of photoelectric events alone at 1200 s. The methods that divide each event between two lines gave a higher CNR than the true first interaction crystal, 9.98, because the division lowered the standard deviation in white matter by 9 to 10% and the contrast by 1 to 2%. Among the methods that assign each event to one line, which gave the same gray matter SNR, the CNR followed the contrast, with 9.98 for the true first interaction crystal, 9.90 for the min-E method and 9.38 for the max-E method.

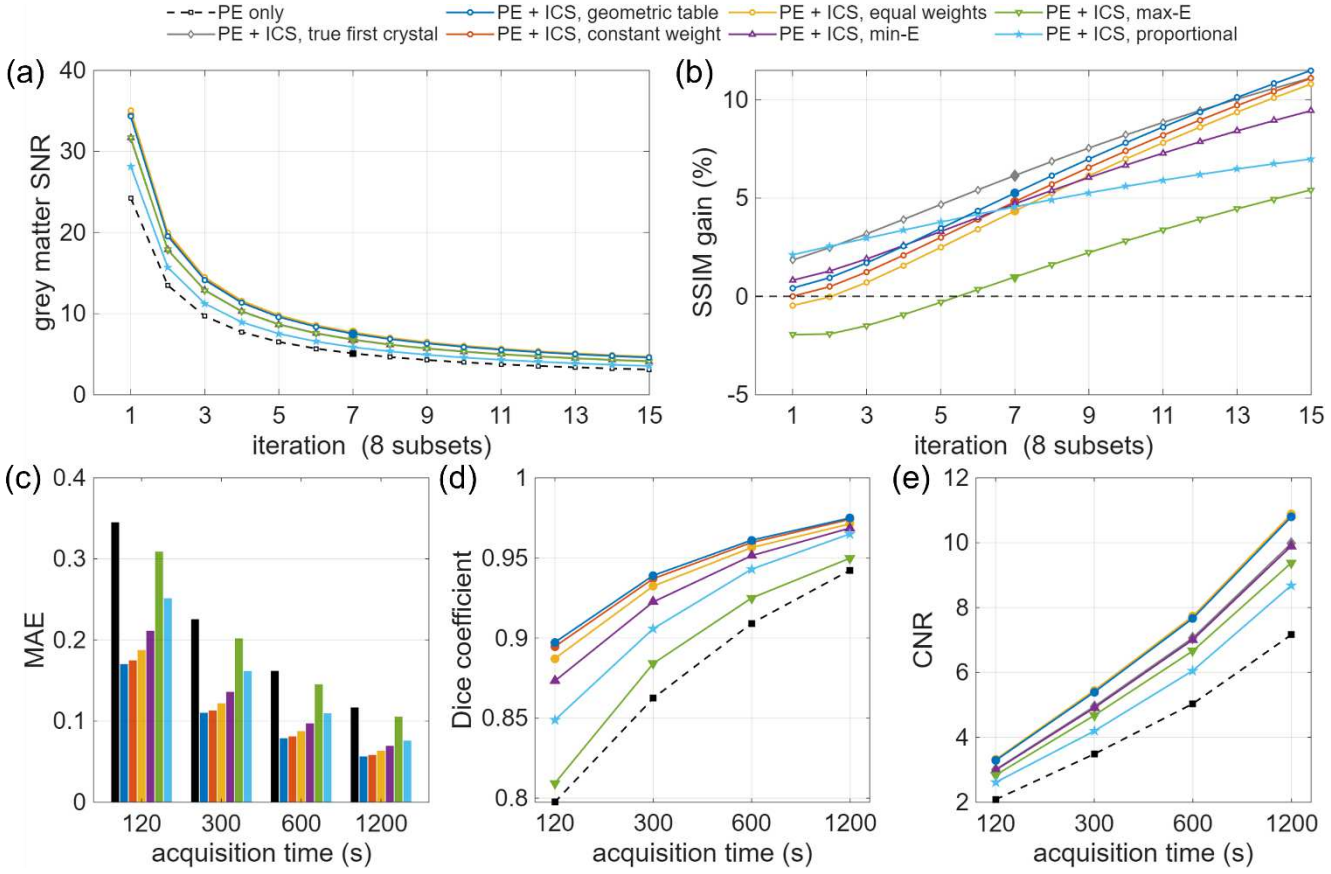


Figure 6. Image quality evaluation results of the Hoffman phantom. (a) Gray matter SNR and (b) SSIM gain over photoelectric events alone against iteration at 1200 s. (c) MAE and (d) Dice coefficient against the image from the true first interaction crystal and (e) CNR between gray matter and white matter against acquisition time at seven iteration

Discussion

Advantages of Probabilistic ICS Positioning

The principal advantage of the proposed method lies in improving the accuracy of the recovered LOR count distributions rather than identifying the first interaction crystal for each ICS event. By assigning geometry-dependent probabilistic weights to the two candidate LORs of a two-crystal ICS event, the method accounts for the uncertainty in the interaction sequence without committing each event to a potentially incorrect LOR. This approach consistently improved LOR count accuracy across the three evaluated phantoms and produced reconstructed images that were closest to those obtained using the true first interaction crystals among the practical methods evaluated.

The distinction between event classification and probabilistic LOR weighting is important. Thresholding the tabulated probability at 0.5, so that each event is committed to a single crystal, identifies the first interaction correctly in 67.7% of events. The rule that assigns every event to the crystal recording the smaller energy reaches 67.8%[14]. The tabulated probability exceeds 0.5 only in configurations carrying 0.96% of the acquisition. For every other event, thresholding at 0.5 selects the crystal with the smaller energy, so the two procedures coincide over 99% of the data. Thus, the geometric information provides little additional benefit for binary classification. What it provides instead is the division of the count between the two candidate LORs, which a classifier does not produce at all, and the evaluation was carried out on recovered counts for that reason rather than on the fraction of events assigned correctly.

DOI, the quantity most often proposed to break the ambiguity[22,23], is limited in much the same way. Assigning each event to the shallower of its two crystals, with depths taken from the simulation with perfect DOI resolution, is correct for 69.9% to 70.7% of events across the three phantoms against 67.8% to 68.0% for the energy rule, and supplying the energy ordering in addition to exact depths changes nothing further. The rule fails mainly when the photon scatters sideways or backward, so that the second interaction lies at a similar or smaller depth. Exact knowledge of a quantity that no current detector measures is thus worth somewhat over two percentage points.

To see why exact depths add so little, we examined how far apart the two interactions were in depth in our hot–cold simulation, using the interaction positions recorded. In the hot–cold phantom the two interaction depths differ by a median of 1.29 mm, and by more than 1 mm in 57.8% of events. Within that subset the depth rule is correct in 82.2% of cases, and within the 11.9% of events separated by more than 5 mm, in 98.7%. Accuracies near 80% are therefore reachable from DOI information[16,18,21,26], but on

a favorably separated subset rather than on the population, and the selection presupposes a detector able to measure the separation in the first place. Since the same rule differs by more than 10% between all events and such a subset, a reported accuracy carries little meaning without the population on which it was obtained.

An additional source of ambiguity is that a two-crystal ICS event need not consist of a single Compton scatter followed by photoelectric absorption. Multiple interactions may occur within the same crystal and remain unresolved in the detector readout. In such cases, the measured energy and DOI may reflect multiple unresolved interactions within the same crystal. Interpreting these measurements as the energy deposit and position of a single Compton interaction can therefore yield an inferred scattering geometry that does not correspond to the actual photon trajectory, potentially leading to incorrect identification of the first interaction crystal even in the absence of measurement uncertainty. This provides further motivation for the proposed probabilistic LOR weighting, which accounts for uncertainty in the first interaction crystal without requiring a unique event-by-event assignment.

Impact of Geometry-Dependent Weighting on LOR Count Recovery

Most of the gain over deterministic assignments comes from dividing the count at all. For the uniform phantom at 1200 s, the RMSE fell by 3.6 percentage points from the min-E method to equal weights, by a further 2.8 to the constant weight and by 1.0 to the geometric table.

The constant-weight implementation, obtained by averaging the geometry-dependent probabilities over the simulated normalization acquisition, retained much of the performance of the full geometric table. The difference between the two implementations was 0.43 to 0.55 percentage points in L_1 at 1200 s across the three phantoms, and two features of the statistics account for this. Most events sit where the geometry matters little. Configurations in which the two crystals are adjacent or diagonal hold 80.8% of the acquisition, with mean probabilities of 0.407 for adjacent and 0.280 for diagonal pairs, against a global value of 0.326, and an event-weighted departure of 0.082. Where the geometry matters most, at large crystal separations with probabilities falling to 0.02, few events are found. A constant weight following the geometry can therefore differ from a constant only slightly over the bulk of an acquisition.

Nevertheless, the geometry-dependent probability varies substantially across individual configurations, particularly with crystal separation and incident photon direction. At oblique incidence, the probability differed by a factor of 1.8 between the two sides of the scattering crystal, demonstrating that a single

constant weight cannot fully describe the geometric dependence of ICS events. The relatively small improvement in the overall L1 error therefore reflects the distribution of events across geometric configurations rather than the absence of geometric dependence.

In the reconstructed images, adding the ICS events improved every quality measure mainly through the 76% increase in counts, because a wrongly assigned LOR shares C0 with the correct one and is usually displaced by one crystal, which is less than the spatial resolution of the image. The effect of the assignment itself appeared most clearly against the image reconstructed with the true first interaction crystal, where the geometric table was closest at every acquisition time.

Together, these results demonstrate the practical value of geometry-dependent probabilistic ICS positioning. The method improves the recovery of LOR count distributions and the agreement of reconstructed images with those from the true first interaction crystal, while requiring only a precomputed probability table and a single lookup per event. Its ability to use a normalization-derived table across different activity distributions offers a practical approach to ICS recovery without target-specific calibration. Furthermore, the relatively small performance difference between geometry-dependent and constant weighting suggests that a single constant weight estimated from a normalization acquisition may also provide a simple and effective alternative when computational simplicity is prioritized over the additional accuracy offered by geometry-dependent weighting.

Limitations and Future Directions

The present study focused on selected ICS events under controlled simulation conditions, leaving several aspects of practical PET measurements for future investigation. Random coincidences were excluded from the analysis, only singles originating from the same annihilation being paired, and their effect on the estimation and on the application of the table is unknown. Coincidences scattering at both ends, or involving more than two crystals at either end, were left out, though they carry a further part of the sensitivity that ICS makes available. The images were evaluated for a single phantom with a binary gray matter pattern and no activity in white matter, unlike the four to one ratio of the physical phantom, without TOF (time-of-flight) information and without scatter correction, and the differences between the assignment methods in the images were small. The intrinsic radioactivity of ^{176}Lu in the crystals was not simulated. Its gamma rays rarely produce coincidences within the 450–550 keV windows, but in measured data they add to the random coincidences.

The numerical values are in any case specific to the scanner modeled here. Crystal pitch governs both the fraction of events that scatter between crystals and the asymmetry of the energy deposition, so a detector of different pitch will yield different figures from the same procedure. The normalization acquisition from which the table was estimated was likewise free of random coincidences and of scatter beyond that of the phantom itself, whereas a measured scan would not be, and the resulting perturbation has not been assessed.

Two sources of information present in the same events were left unused. The partition of energy between the crystals is measured but enters only through its ordering, so that an event depositing 250 and 261 keV is treated exactly as one depositing 80 and 431 keV. The DOI constrains the direction of the incident photon far more tightly than the crystal indices do and is available in depth-encoding detectors[22,24], although its contribution to the choice of crystal is bounded as shown above. Whether a weight conditioned on either quantity recovers the distribution more closely than geometry alone is the question we intend to address next.

The present study relied on Monte Carlo simulations because accurate evaluation of the proposed weighting method requires knowledge of the true first interaction crystal for each ICS event, which is not directly available in measured PET data. The simulations provided this ground truth, allowing quantitative evaluation of LOR count recovery and reconstructed image quality against the true first interaction crystal. Future work will therefore investigate whether the simulation-derived probabilities can be reliably applied to experimental PET data and remain robust across different source distributions.

Conclusion

In summary, dividing an ICS count between its two candidate LORs according to a probability conditioned on the detector geometry, rather than on the activity distribution, gave the most accurate LOR counts among the practical methods in three phantoms. The probability depends strongly on the position of the opposing crystal and differs by a factor of 1.8 between the two sides of the scattering crystal at oblique incidence. A single table estimated once from a cylindrical normalization acquisition performed equally across a uniform distribution, a four to one rod contrast and a brain pattern, and a table estimated from 960 s of the target acquisition itself did not exceed its accuracy. In reconstructed images, the table gave the images closest to those obtained with the true first interaction crystal. The division of the count is thus a property of the scanner rather than of the subject, and it can be applied to list mode data through one table lookup per event, with no measurement beyond the normalization scan.

Methods

Mathematical Modeling of ICS Probability

Each ICS event is treated as a binary random variable that indicates whether the first interaction occurred in C_1 or C_2, where C_1 denotes the crystal with the higher deposited energy. The energies measured in C_1 and C_2 are written E_1 and E_2, so that $E_1 > E_2$. For a fixed opposing crystal C_0, the event has two possible LORs, (C_0, C_1) and (C_0, C_2), and

$$X = \begin{cases} 1, if\ C_f = C_1, \\ 0, if\ C_f = C_2, \end{cases} \quad X \sim \text{Bernoulli (p)} \tag{1}$$

where C_f is the first interaction crystal and p is the probability that $C_f = C_1$ for the given geometric configuration (C_0, C_1, C_2). The incident photon has an energy E = 511 keV and arrives from the direction of C_0. At a point r in the first crystal, its direction $\hat{u}_0$ is fixed by the positions of C_0 and r.

The probability density for Compton scattering through the angle θ, measured from $\hat{u}_0$, is given by the normalized Klein–Nishina distribution[32]:

$$\mathrm{K}(\theta \mid E) = \frac{1}{\sigma_C(E)} \frac{d\sigma_C}{d\Omega}(E, \theta) = \frac{1}{\sigma_C(E)} \frac{r_e^2}{2} \left(\frac{E'}{E}\right)^2 \left(\frac{E'}{E} + \frac{E}{E'} - sin^2\theta\right) \tag{2}$$

where r_e is the classical electron radius, $\sigma_c(E)$ is the total Compton cross section and E' is the energy of the scattered photon given by the Compton equation below.

$$E' = \frac{E}{1 + \frac{E}{m_0 c^2}(1 - cos\,\theta)} \tag{3}$$

, where m_0 is electron rest mass and c is speed of light.

For a photon scattered at r in crystal C_i into the direction Ω, the probability that it reaches the other crystal C_j and is absorbed there is

$$\Phi_{i \to j}(r, \Omega; E, \theta) = \mathbf{I}_{i \to j}(r, \Omega) e^{-\mu(E')l_{path}} (1 - e^{-\mu(E')L}) \pi_{pe}(E') \tag{4}$$

where $I_{i \to j}(r, \Omega)$ equals 1 when the scattered trajectory intersects C_j and 0 otherwise, $\mu(E')$ is the total attenuation coefficient, l_{path} is the distance from r to the surface of C_j, L is the chord length of the trajectory inside C_j and $\pi_{pe}(E') = \mu_{pe}(E') / \mu(E')$ is the photoelectric fraction. Equation (4) treats the absorption in C_j as a single interaction.

The energy ordering $E_1 > E_2$ restricts the scattering angles allowed in each case. With E = 511 keV, the scattered photon carries less than 255.5 keV when $\theta > 90°$ and more when $\theta < 90°$. When the photon scatters first in C_1, C_1 receives the recoil energy 511 keV − E' and C_2 receives E', so $E_1 > E_2$ requires $\theta >$

90°. When it scatters first in C_2, $E_1 = E'$ and $E_2 = 511\ \text{keV} - E'$, so $E_1 > E_2$ requires $\theta < 90°$. The contribution of the first sequence is

$$\Lambda_{1\to2}(E) = \mu_C(E) \int_{V_1} e^{-\mu(E)s_{in}(r)} \left[\int_{4\pi} K(\theta \mid E)\Phi_{1\to2}(r, \Omega; E, \theta)\mathbf{I}(\theta > 90°)d\Omega \right] dV \qquad (5)$$

where V_1 is the volume of C_1, $\mu_C(E)$ is the linear attenuation coefficient for Compton scattering at energy E, $s_{in}(r)$ is the path length of the incident photon inside the detector before it reaches r and $\mathbf{I}(\cdot)$ is the indicator function. The outer integral runs over the volume of C_1 and the inner integral over all directions Ω of the scattered photon, a solid angle of 4π. $\Lambda_{2\to1}$ is obtained in the same way over the volume V_2 of C_2, with $\mathbf{I}$ ($\theta < 90°$).

The probability that C_1 is the first interaction crystal is then

$$p = \frac{\Lambda_{1\to2}(E)}{\Lambda_{1\to2}(E) + \Lambda_{2\to1}(E)} \qquad (6)$$

Equation (6) depends only on the positions of C_0, C_1 and C_2 and on the interaction physics in the detector. The incident direction and the path of the incident photon inside the detector change with the position of C_0, so p depends on the opposing crystal as well as on the pair (C_1, C_2). Because Compton scattering at 511 keV favors forward angles, the sequence that requires $\theta > 90°$ is less likely, and p is below 0.5 for most configurations. For a given configuration p does not depend on the imaging target, except for photons scattered in the object, whose incident direction differs from the direction of C_0.

Probability Estimation and LOR Weighting

The conditional probability p was estimated from a simulated normalization acquisition (see Simulation setup) rather than directly calculated from equation (6). The estimated probabilities were tabulated as a function of the transaxial and axial separations between the two interacting crystals and the position of the opposing crystal. The table is then applied on an event-by-event basis. For each ICS coincidence the two candidate LORs, (C_0, C_1) and (C_0, C_2), are formed, with C_1 denoting the crystal that recorded the larger energy. The geometric configuration is evaluated from the three crystal indices, the corresponding probability is retrieved from the table, and the event is added to the two LORs with weights p and $1 - p$. Since the labeling is fixed by the measured energy ordering, a single table is sufficient and no branching on the unknown first interaction crystal is required. The procedure involves one table lookup per event and can therefore be applied to list-mode data as they are acquired.

Simulation Setup and Event Selection

All simulations were performed with GATE v9.2[33]. The detector followed the second-generation

PET*coil* RF-penetrable TOF-PET brain insert[31], consisting of 16 modules per ring, with each module containing a 16 × 8 array of LYSO crystals (3.2 × 3.2 × 20 mm³) at a pitch of 3.26 mm. The simulated system comprised three of the six rings of the scanner, with an inner diameter of 315 mm and an axial field of view of 78.24 mm. An energy resolution of 11.74% FWHM at 511 keV was applied.

Coincidences were formed only between singles originating from the same annihilation, so that random coincidences were excluded from the analysis. A coincidence in which one module recorded exactly two crystals and the other exactly one was classified as an ICS event, and one in which both modules recorded a single crystal was classified as a photoelectric event. Coincidences in which both ends scattered, or in which more than two crystals were involved at either end, were not analyzed. Events were retained when the summed energy of the two scattered crystals and the energy of the opposing crystal both fell within 450–550 keV, and when the two modules were separated by at least a quarter of the ring, since LORs between modules closer than this pass outside the phantom and cannot carry a true coincidence. The first interaction crystal was taken from the Hits file of the GATE simulation as the earliest interaction within the scattering module. Positrons were emitted with the mean kinetic energy of ^{18}F (249.8 keV).

The table of weights was estimated from a normalization acquisition, in which an annular water cylinder of 95 mm inner and 100 mm outer radius and 70 mm length was uniformly filled with ^{18}F at 172.6 kBq/mL, corresponding to 37 MBq, and acquired for 180 s. The hollow interior limits attenuation and object scatter while the shell irradiates all detector pairs.

Three phantoms of differing activity distribution were then simulated, each contained within a water cylinder of 100 mm radius. A uniform phantom of 70 mm length was filled at 16.8 kBq/mL and acquired for 1200 s. A hot–cold phantom of the same dimensions contained two rods of 30 mm radius placed 40 mm either side of the axis, with the background filled at 20.5 kBq/mL, one rod at four times that concentration and the other left inactive[34], acquired for 1200 s. A Hoffman brain phantom was represented by a binary activity map of the two-dimensional Hoffman pattern[35] sampled at 0.98 × 0.98 × 2.0 mm, in which the active voxels covered 649 mL and were filled uniformly at 52.4 kBq/mL, giving 34.0 MBq in total. It was contained in a water cylinder of 80 mm length and acquired for 1200 s. White matter carried no activity.

Evaluation of LOR assignment

Each ICS event was assigned to two candidate LORs, formed by the opposing crystal with each of the two scattered crystals in turn. Lines were binned by the pair of crystal indices. The reference distribution was obtained by placing the whole event on the line containing the true first interaction crystal, and the estimated distribution by dividing it between the two lines according to the weight under test. Bins holding

no true count were excluded, so that weight placed on a line that received no event is registered as a leakage rather than as an error of that bin.

Writing e_i and t_i for the estimated and true counts of a bin i and $r_i = (e_i - t_i)/t_i$ for its relative error, with the sums over i taken over the bins holding true counts, four quantities were computed and compared, each weighted by the true counts:

$$L_1 = \frac{\sum_i |e_i - t_i|}{\sum_i t_i} \tag{7}$$

$$\text{RMSE} = \sqrt{\frac{\sum_i t_i r_i^2}{\sum_i t_i}} \tag{8}$$

$$\text{leakage} = -\frac{\sum_i t_i r_i}{\sum_i t_i} = \frac{\sum_{t_i=0} e_i}{\sum_i t_i} \tag{9}$$

$$\text{SD} = \sqrt{\text{RMSE}^2 - \text{leakage}^2} \tag{10}$$

L_1 represents the normalized absolute error in the estimated LOR counts (equation (7)), while RMSE quantifies the count-weighted relative error (equation (8)). The leakage represents the fraction of estimated counts assigned to LORs with no true event (equation (9)). Because the true counts are by construction confined to the retained bins while the estimated counts are not, the leakage is exactly the negative of the count weighted mean of r, and SD is the remaining spread over the bins with true counts (equation (10)). All quantities are reported as percentages and as a function of acquisition time. The leakage falls as the acquisition lengthens, since fewer lines remain without true counts.

The proposed geometry-dependent probabilistic weighting framework was evaluated in two implementations: geometric table, which uses the probability corresponding to each event's geometric configuration, and constant weighting, which uses a single probability ($\bar{p}$) obtained as the event-weighted mean of these probabilities from the same simulated normalization acquisition. These two implementations were compared with four reference methods. Two are deterministic, assigning the event entirely to the crystal recording the smaller energy (min-E) or to the crystal recording the larger energy (max-E). One is constant across all events, equal weights of one half (equal weight). The last is the proportional method[12] with the weights computed from the photoelectric events of the same acquisition and set to one half when neither LOR recorded a photoelectric event.

Finally, for the proposed method, to establish whether the geometric dependence is better obtained from a normalization scan than from the target acquisition itself, each phantom acquisition was divided into a training and a test set in a ratio of four to one (960 s to 240 s). Data were then estimated from the leading part of the training set at durations of 7.5, 15, 30, 60, 120 240, 480, and 960 s, and each was scored on the same test set, which was never used for estimation.

Image Reconstruction and image quality

Images of the Hoffman phantom were reconstructed at acquisition times of 120, 300, 600 and 1200 s. The photoelectric events alone served as the baseline, and the ICS events were added to them with each of the assignment methods compared in the evaluation of LOR assignment and with the true first interaction crystal. Images from ICS events alone were not evaluated, because in practice ICS events are reconstructed together with photoelectric events. The energy windows, the energy ordering and the separation of at least a quarter of the ring were the same as in the evaluation of LOR assignment.

Images were reconstructed with OSEM[36] using 8 subsets grouped by the azimuthal angle of the LOR, for up to 15 iterations. The system matrix was computed on the fly with a Joseph projector[37] on a grid of $140 \times 140 \times 50$ voxels of 1.6 mm, half the crystal width. Each LOR joined the centers of its two crystals at a radius of 163 mm, the mean depth of interaction of photoelectric events. Attenuation was modeled with the water cylinder of the phantom ($\mu = 0.0096$ mm^{-1}). Random coincidences were excluded by keeping only coincidences whose two singles came from the same decay, and coincidences scattered in the phantom were kept without correction.

The detector efficiency of each LOR was estimated from the 1200 s acquisition of the uniform phantom, using only coincidences that were not scattered in the phantom. LORs related by the rotational and mirror symmetries of the scanner were grouped, and for each group the efficiency was taken as the ratio of the measured counts to the counts expected from the chord length through the cylinder with attenuation. Efficiencies were estimated separately for the photoelectric events and for the ICS events of each assignment method, in the same way as a scanner is normalized with the positioning method it uses. The efficiency varied by a factor of more than four with the distance of the LOR from the center, because oblique LORs see a wider crystal face, so a correction for crystal efficiency alone was not sufficient. LORs that did not pass through the uniform cylinder were excluded.

Images were evaluated in the 25 central slices ($|z| \leq 20$ mm), over which the phantom does not change along the axis. Gray matter was taken from the activity map, resampled to the image grid and thresholded at one half, so the same mask was used for every image. Each image was divided by its mean over the brain region, obtained by closing the gray matter mask with a disk of 8 mm radius and filling the holes. The gray matter SNR was the mean activity in gray matter divided by the standard deviation across slices averaged over gray matter. White matter was taken as the pixels of the brain region at least 2 mm from gray matter. The CNR was the difference between the mean activity in gray matter and in white matter, divided by the standard deviation across slices averaged over white matter. Because white matter carried no activity, the true contrast was known, and the activity measured in white matter came only from blurring, object scatter and misassigned events. SSIM[38] was computed against the true activity slice by slice, with a Gaussian window of 1.5 pixels, $K1 = 0.01$ and $K2 = 0.03$. To isolate the effect of the assignment, each image was also compared with the image reconstructed from the same events with the

true first interaction crystal. The MAE was computed over the brain region. For the Dice coefficient[39], gray matter was segmented in each slice with a threshold halfway between the mean activity of gray matter and of white matter in that image, and the coefficient was averaged over the slices. Values are reported at seven iterations.

Use of large language models

Claude (Anthropic) was used to edit the language of the manuscript and to help write code for the data analysis, image reconstruction and plotting. The authors checked all text and code produced with its help and take full responsibility for the content of the manuscript.

Data availability

All data supporting the findings of this study were generated using GATE (version 9.2) and are available from the corresponding author upon reasonable request.

References

1. Levin, C. S. & Zaidi, H. Current trends in preclinical PET system design. *PET Clin.* **2**, 125–160 (2007).

2. Lee, J. S. & Lee, M. S. Advancements in positron emission tomography detectors. *PET Clin.* **19**, 1–24 (2024).

3. Gu, Z. et al. Performance evaluation of HiPET, a high sensitivity and high resolution preclinical PET tomograph. *Phys. Med. Biol.* **65**, 045009 (2020).

4. Kang, H. G. et al. Submillimeter-resolution PET for high-sensitivity mouse brain imaging. *J. Nucl. Med.* **64**, 978–985 (2023).

5. Son, J.-W. et al. SimPET: a preclinical PET insert for simultaneous PET/MR imaging. *Mol. Imaging Biol.* **22**, 1208–1217 (2020).

6. Shao, Y., Cherry, S. R., Siegel, S. & Silverman, R. W. A study of inter-crystal scatter in small scintillator arrays designed for high resolution PET imaging. *IEEE Trans. Nucl. Sci.* **43**, 1938–1944 (1996).

7. Zhang, C., Sang, Z., Wang, X., Zhang, X. & Yang, Y. The effects of inter-crystal scattering events on the performance of PET detectors. *Phys. Med. Biol.* **64**, 205004 (2019).

8. Hsu, D. F. C., Freese, D. L., Innes, D. R. & Levin, C. S. Intercrystal scatter studies for a 1 mm^3 resolution clinical PET system prototype. *Phys. Med. Biol.* **64**, 095024 (2019).

9. Saaidi, R., Rodriguez-Villafuerte, M., Alva-Sanchez, H. & Martinez-Davalos, A. Crystal scatter effects in a large-area dual-panel Positron Emission Mammography system. *PLoS ONE* **19**, e0297829 (2024).

10. Lee, M. S., Shim, H. S. & Lee, J. S. Strategies for mitigating inter-crystal scattering effects in positron emission tomography: a comprehensive review. *Biomed. Eng. Lett.* **14**, 1243–1258 (2024).

11. Gillam, J. E. et al. Sensitivity recovery for the AX-PET prototype using inter-crystal scattering events. *Phys. Med. Biol.* **59**, 4065–4083 (2014).

12. Lage, E. et al. Recovery and normalization of triple coincidences in PET. *Med. Phys.* **42**, 1398–1410 (2015).

13. Michaud, J. B. et al. Sensitivity increase through a neural network method for LOR recovery of ICS triple coincidences in high-resolution pixelated-detectors PET scanners. *IEEE Trans. Nucl. Sci.* **62**, 82–94 (2015).

14. Comanor, K. A., Virador, P. R. G. & Moses, W. W. Algorithms to identify detector Compton scatter in PET modules. *IEEE Trans. Nucl. Sci.* **43**, 2213–2218 (1996).

15. Surti, S. & Karp, J. S. Impact of event positioning algorithm on performance of a whole-body PET scanner using one-to-one coupled detectors. *Phys. Med. Biol.* **63**, 055008 (2018).

16. Rafecas, M. et al. Inter-crystal scatter in a dual layer, high resolution LSO-APD positron emission tomograph. *Phys. Med. Biol.* **48**, 821–848 (2003).

17. Lee, M. S., Kang, S. K. & Lee, J. S. Novel inter-crystal scattering event identification method for PET detectors. *Phys. Med. Biol.* **63**, 115015 (2018).

18. Lee, S. & Lee, J. S. Inter-crystal scattering recovery of light-sharing PET detectors using convolutional neural networks. *Phys. Med. Biol.* **66**, 185004 (2021).

19. Lee, S. & Lee, J. S. Experimental evaluation of convolutional neural network-based inter-crystal scattering recovery for high-resolution PET detectors. *Phys. Med. Biol.* **68**, 095017 (2023).

20. Shim, H., Bae, S., Lee, S. & Lee, J. Inter-crystal scattering event identification using a novel silicon photomultiplier signal multiplexing method. *Phys. Med. Biol.* **68**, 115008 (2023).

21. Petersen, E., LaBella, A., Li, Y., Wang, Z. & Goldan, A. H. Resolving inter-crystal scatter in a light-sharing depth-encoding PET detector. *Phys. Med. Biol.* **69**, 035024 (2024).

22. Ito, M., Hong, S. J. & Lee, J. S. Positron emission tomography (PET) detectors with depth-of-interaction (DOI) capability. *Biomed. Eng. Lett.* **1**, 70–81 (2011).

23. Gu, Z. et al. A DOI detector with crystal scatter identification capability for high sensitivity and high spatial resolution PET imaging. *IEEE Trans. Nucl. Sci.* **62**, 740–747 (2015).

24. LaBella, A. et al. High-resolution depth-encoding PET detector module with prismatoid light-guide array. *J. Nucl. Med.*

61, 1528–1533 (2020).

25. Abbaszadeh, S., Chinn, G. & Levin, C. S. Positioning true coincidences that undergo inter- and intra-crystal scatter for a sub-mm resolution cadmium zinc telluride-based PET system. *Phys. Med. Biol.* **63**, 025012 (2018).

26. Pratx, G. & Levin, C. S. Bayesian reconstruction of photon interaction sequences for high-resolution PET detectors. *Phys. Med. Biol.* **54**, 5073–5094 (2009).

27. Gross-Weege, N., Schug, D., Hallen, P. & Schulz, V. Maximum likelihood positioning algorithm for high-resolution PET scanners. *Med. Phys.* **43**, 3049–3061 (2016).

28. Lee, S., Kim, K. Y., Lee, M. S. & Lee, J. S. Recovery of inter-detector and inter-crystal scattering in brain PET based on LSO and GAGG crystals. *Phys. Med. Biol.* **65**, 195005 (2020).

29. Lee, S., Lee, M. S., Kim, K. Y. & Lee, J. S. Systematic study on factors influencing the performance of interdetector scatter recovery in small-animal PET. *Med. Phys.* **45**, 3551–3562 (2018).

30. Dong, Q. et al. The PETcoil project: PET performance evaluation of two detector modules for a second generation RF-penetrable TOF-PET brain dedicated insert for simultaneous PET/MRI. *Phys. Med. Biol.* **68**, 085010 (2023).

31. Dong, Q. et al. PETcoil: first results from a second-generation RF-penetrable TOF-PET brain insert for simultaneous PET/MRI. *Phys. Med. Biol.* **69**, 185007 (2024).

32. Knoll, G. F. *Radiation Detection and Measurement* 4th edn (John Wiley & Sons, 2010).

33. Jan, S. et al. GATE: a simulation toolkit for PET and SPECT. *Phys. Med. Biol.* **49**, 4543–4561 (2004).

34. Torres-Espallardo, I., Rafecas, M., Spanoudaki, V., McElroy, D. P. & Ziegler, S. I. Effect of inter-crystal scatter on estimation methods for random coincidences and subsequent correction. *Phys. Med. Biol.* **53**, 2391–2411 (2008).

35. Harrison, R. L. et al. Technical Note: A digital reference object representing Hoffman's 3D brain phantom for PET scanner simulations. *Med. Phys.* **47**, 1174–1180 (2020).

36. Hudson, H. M. & Larkin, R. S. Accelerated image reconstruction using ordered subsets of projection data. *IEEE Trans. Med. Imaging* **13**, 601–609 (1994).

37. Joseph, P. M. An improved algorithm for reprojecting rays through pixel images. *IEEE Trans. Med. Imaging* **1**, 192–196 (1982).

38. Wang, Z., Bovik, A. C., Sheikh, H. R. & Simoncelli, E. P. Image quality assessment: from error visibility to structural similarity. *IEEE Trans. Image Process.* **13**, 600–612 (2004).

39. Dice, L. R. Measures of the amount of ecologic association between species. *Ecology* **26**, 297–302 (1945).

Funding

This work was supported by a grant from the Korea Medical Device Development Foundation (KMDF), funded by the Korean government (the Ministry of Science and ICT, the Ministry of Trade, Industry and Resources, the Ministry of Health and Welfare, and the Ministry of Food and Drug Safety) (Project Numbers: 2410019162, RS-2026-25540876) and the Korea Institute of Energy Technology Evaluation and Planning(KETEP) and the Ministry of Climate, Energy & Environment(MCEE) of the Republic of Korea (No. RS-2026-25537883).

Author contributions

H.S.S. conceived the study, performed the simulations and the analysis and wrote the manuscript. M.N.U. provided the detector model of the PET*coil* insert. J.S.L., C.S.L. and G.B.K. supervised the study. All authors reviewed the manuscript.

Competing interests

The authors declare no competing interests.